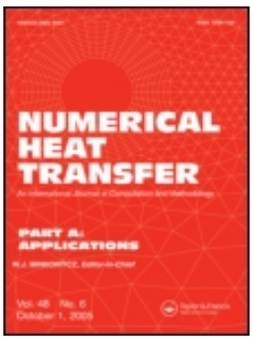

Taylor & Francis
Taylor & Francis Group

Numerical Heat Transfer, Part A: Applications
An International Journal of Computation and Methodology

ISSN: 1040-7782 (Print) 1521-0634 (Online) Journal homepage: https://www.tandfonline.com/loi/unht20

A 3D Total Variation Diminishing Scheme for Compositional Reservoir Simulation Using the Element-Based Finite-Volume Method

Bruno Ramon Batista Fernandes , Alysson Daniel Ribeiro Gonçalves , Edilson Pimentel Drumond Filho , Ivens da Costa Menezes Lima , Francisco Marcondes & Kamy Sepehrnoori

To cite this article: Bruno Ramon Batista Fernandes , Alysson Daniel Ribeiro Gonçalves , Edilson Pimentel Drumond Filho , Ivens da Costa Menezes Lima , Francisco Marcondes & Kamy Sepehrnoori (2015) A 3D Total Variation Diminishing Scheme for Compositional Reservoir Simulation Using the Element-Based Finite-Volume Method, Numerical Heat Transfer, Part A: Applications, 67:8, 839-856, DOI: 10.1080/10407782.2014.949196

To link to this article: https://doi.org/10.1080/10407782.2014.949196

Published online: 20 Dec 2014.

Submit your article to this journal

Article views: 142

View related articles

View Crossmark data

Citing articles: 5 View citing articles

Full Terms & Conditions of access and use can be found at
https://www.tandfonline.com/action/journalInformation?journalCode=unht20

Numerical Heat Transfer, Part A, 67: 839–856, 2015
Copyright © Taylor & Francis Group, LLC
ISSN: 1040-7782 print/1521-0634 online
DOI: 10.1080/10407782.2014.949196

Taylor & Francis
Taylor & Francis Group

A 3D TOTAL VARIATION DIMINISHING SCHEME FOR COMPOSITIONAL RESERVOIR SIMULATION USING THE ELEMENT-BASED FINITE-VOLUME METHOD

Bruno Ramon Batista Fernandes[1], Alysson Daniel Ribeiro Gonçalves[1], Edilson Pimentel Drumond Filho[1], Ivens da Costa Menezes Lima[1], Francisco Marcondes[2], and Kamy Sepehrnoori[3]

[1]*Laboratory of Computational Fluid Dynamics, Federal University of Ceará, Ceará, Brazil*

[2]*Department of Metallurgical Engineering and Material Science, Federal University of Ceará, Ceará, Brazil*

[3]*Department of Petroleum and Geosystems Engineering, The University of Texas at Austin, Austin, Texas, USA*

Interpolation function is a key parameter for numerical simulation using finite-difference, finite-element, and finite-volume methods, especially when the advective terms of the conservation equations are considered. Due to the flow orientation, a first-order interpolation scheme such as upwind introduces a considerable degree of numerical diffusion in the numerical solution. In this work, we present a second-order total variation diminishing scheme in conjunction with 3D compositional reservoir simulation using the element-based finite-volume method (EbFVM). The results of several case studies using the hexahedron element are shown in terms of oil, water, and gas production, as well as saturation field.

1. INTRODUCTION

Numerical schemes such as the finite-difference, finite-element, and finite-volume methods require an evaluation of certain physical properties at different spatial positions in the computational domain. In general, when using unstructured grids the physical properties such as pressure, temperature, and number of moles are stored at the vertices of each element. In order to evaluate any of these properties inside the element, some interpolation function needs to be used. The way this interpolation is performed has a major impact on the numerical solution and on determining the grid refinement, and also in giving rise to numerical dispersion,

Received 3 March 2014; accepted 24 July 2014.

The authors thank Dr. Chowdhury K. Mamun for his comments on this manuscript.

Address correspondence to Francisco Marcondes, Department of Metallurgical Engineering and Material Science, Federal University of Ceará, Campus do Pici, Bloco 729 Fortaleza, Ceará, Brazil 60455-760. E-mail: marcondes@ufc.br

Color versions of one or more of the figures in the article can be found online at www.tandfonline.com/unht.

NOMENCLATURE

A	area, m^2
Acc	accumulation term
F	advective plus diffusive transport
c_f	rock compressibility, Pa^{-1}
d	distance, m
f	fugacity, Pa
$\bar{\bar{k}}$	absolute permeability tensor, m^2
$\bar{\bar{K}}_{ij}$	dispersion tensor, m^2/s
k_r	relative permeability
N	trilinear shape function or number of moles, mol
N_v	total number of vertices
n_c	number of components
n_p	number of phases
P	pressure, Pa
q	well volumetric rate, mol/s
r	successive slope ratio
S	saturation
t	time, s
V_b	bulk volume, m^3
V_p	pore volume, m^3
V_t	total fluid volume, m^3
$\overline{V}_{tk}$	partial molar volume, m^3/mol
x	phase mole fraction
z	overall composition
Δ	any physical property evaluated at the vertex
δ	any physical property evaluated at the interface
ξ	mole density, mol/m^3
φ	porosity
λ	phase mobility, $(Pa \cdot s)^{-1}$
Φ	hydraulic potential, Pa
ψ	nonlinear function of successive slope ratio
γ	specific gravity, Pa/m
μ	viscosity, $Pa \cdot s$

Subscripts

i	control volume, vertex, or component
j	phase
U	upwind vertex
w	water component
r	reference phase

Superscripts

0	property evaluated on the previous time occasion

nonphysical oscillations, and other types of error. Consequently, an interpolation function that can take into account the correct variation of fluid flow and discontinuities, while maintaining numerical stability, can reduce computational time and obtain accurate numerical solutions.

Baliga and Patankar [1] introduced the control-volume finite-element method (CVFEM) in conjunction with triangular elements for the solution of advective–diffusive problems, which in turn gave rise to the cell–vertex approach. They used the upwind and the exponential interpolation functions to evaluate the gradients and physical properties of the integration points. The exponential method uses shape functions which are exponential in the direction of the element's average velocity and linear in the normal direction. This method is known as flow-oriented interpolation (FLO). CVFEM was later renamed the element-based finite-volume method (EbFVM) [2]. Since EbFVM only borrows the element details and shape functions from the finite-element method but still performs a material balance in order to obtain the approximated equations, in this work we will use the later denomination of EbFVM. Prakash [3] extended the FLO scheme to take into account the source terms—this new scheme is called FLOS. In aiming to improve skewed grids, many other schemes have been developed. These were first based on the skew upwind techniques proposed by Raithby [4, 5] for regular grids. Hassan et al. [6] and Schneider and Raw [7] developed the skew upwind for triangular and quadrilateral grids, respectively. Swaminathan and Voller [8, 9] extended the streamline upwind Petrov–Galerkin (SUPG) scheme of Brooks and Hughes [10] to EbFVM. This method is termed

streamline upwind control volume (SUCV) and uses streamline to evaluate the upwind influence. Although some of these methods can produce second-order accuracy, such as SUCV, they provide stable solutions only for first-order accuracy and in general require special treatment to avoid any downwind influence.

Another class of scheme is the total variation diminishing (TVD) methods that are known to preserve monotonicity, with higher-order TVD schemes increased accuracy. The first flux limiter to preserve monotonicity for one-dimensional advective problems was developed by Van Leer [11]. The principles behind the preservation of monotonicity in the TVD scheme were later investigated by Harten [12]. Subsequently, the TVD region for one dimension in equally spaced meshes was formulated by Sweby [13], who proved that the limiters of Van Leer, Roe [14], and Chakravarthy and Osher [15] follow the TVD definition. Sweby [13] also showed that the Lax–Wendroff [16] and Warming–Beam [17] schemes do not follow the TVD definition.

Several works have adapted the TVD interpolation function from structured to unstructured grids [18–25]. However, most of these efforts were addressed to cell-centered grids. Although few authors have suggested that their schemes would also work for cell–vertex discretization, these were all constructed and applied to cell-centered unstructured grids. Fernandes et al. [26] recently extended the idea of Darwish and Moukalled [20] from 2D cell-centered grids to 2D unstructured grids using EbFVM in conjunction with compositional reservoir simulation using an implicit pressure explicit composition (IMPEC) approach. To the best of our knowledge, no higher-order TVD interpolation function has been used to date in conjunction with 3D cell–vertex unstructured meshes. In this work, we investigate the upwind and TVD methods presented by Fernandes et al. [26] for 3D unstructured meshes. These interpolation functions are implemented in an in-house compositional reservoir simulator called UTCOMP [27, 28]. UTCOMP was developed at the Center for Petroleum and Geosystems Engineering at The University of Texas at Austin for the simulation of enhanced recovery processes. UTCOMP formulation is based in an IMPEC approach, multiphase/multicomponent compositional equation of a state simulator which can handle the simulation of several enhanced oil recovery processes. EbFVM implemented into the UTCOMP simulator is based on the works of Marcondes and Sepehrnoori [29], Marcondes et al. [30], and Santos et al. [31].

2. PHYSICAL MODEL

Isothermal, multicomponent, multiphase fluid flow in porous media can be modeled using three types of equation: material balance, fluid phase equilibrium, and constraint (see Refs. [27, 28]).

A material balance equation is required for each component in the system. In reservoir modeling, the phase velocities are usually approximated by a multiphase version of Darcy's law. The material balance equation for the i-th component for a full symmetric absolute permeability tensor can be written as

$$\frac{1}{V_b}\frac{\partial N_i}{\partial t} - \vec{\nabla}\cdot\left[\sum_{j=1}^{n_p}\xi_j x_{ij}\lambda_j \bar{\bar{k}}\cdot\vec{\nabla}\Phi_j + \phi\sum_{j=1}^{n_p}\xi_j S_j \overline{\overline{K}}_{ij}\cdot\vec{\nabla}x_{ij}\right] - \frac{q_i}{V_b} = 0;\ i = 1,2,\ldots,n_c,n_c+1, \tag{1}$$

where n_c is the number of components except for water, n_c+1 denotes the water component, n_p is the number of phases present in the reservoir, φ is the porosity, N_i is the number of moles of the i-th component, ξ_j and λ_j are the molar density and relative mobility of the j-th phase, respectively, x_{ij} is the mole fraction of the i-th component in the j-th phase, $\bar{\bar{k}}$ is the absolute permeability tensor, $\overline{\overline{K}}_{ij}$ is the physical dispersion tensor, q_i is the molar flow rate of the component i due to well injection/production, V_b is the volume of control-volume, and Φ_j is the hydraulic potential of the j-th phase given by

$$\Phi_j = P_j - \gamma_j Z, \tag{2}$$

where P_j denotes the pressure of the j-th phase and Z is the depth, which is positive in the downward direction.

The nonaqueous phases are assumed to be in equilibrium condition, which can be expressed in terms of the equality of fugacities (f) of the phases, as follows:

$$f_i^j - f_i^r = 0; \quad i = 1, \ldots, n_c; \quad j = 2, \ldots\ldots, n_p. \tag{3}$$

In Eq. (3), $f_i^j = \ln(x_{ij}\,\phi_{ij})$, where φ_{ij} is the fugacity coefficient of component i in the j-th phase, and r denotes the reference phase. The restriction of the molar fraction is used to obtain the solution of Eq. (3):

$$\sum_{i=1}^{n_c} x_{ij} - 1 = 0, \quad j = 2, \ldots, n_p; \quad \sum_{i=1}^{n_c} \frac{z_i(K_i - 1)}{1 + \nu(K_i - 1)} = 0, \tag{4}$$

where z_i is the overall molar fraction of the i-th component, K_i is the equilibrium ratio for the i-th component, and ν is the mole fraction of the gas phase in the absence of water.

Fugacity and PVT (pressure-volume-temperature) properties are evaluated in this work using the Peng–Robinson equation of state [32]. The flash procedure used considers a fixed and known pressure, temperature, and global composition (isothermal flash) in order to evaluate the phase composition and fluid properties. It is worth mentioning that the water component is not included in the flash calculations. Further details of this procedure can be found in Perschke [33].

The closure equation is derived from the volume constraint (i.e., the available pore volume of each cell must be filled by all phases present in the reservoir). This constraint gives rise to the following equation:

$$\sum_{j=1}^{n_p} S_j = 1, \tag{5}$$

where S_j is the saturation of the j-th phase, which is defined as a volumetric fraction.

In the UTCOMP simulator, the unknown primary variables are oil pressure and total number of moles for every component: P, N_1,. . .,N_{nc}, N_{w}. The oil pressure

is obtained through a volume balance and is given by

$$\left(\phi^0 c_f - \frac{1}{V_b}\frac{\partial V_t}{\partial P}\right)\frac{\partial P}{\partial t} = \sum_{k=1}^{n_c} \overline{V}_{tk} \sum_{j=1}^{n_p} \left(\vec{\nabla}\cdot x_{kj}\xi_j \frac{k_{rj}}{\mu_j}\bar{\bar{k}}\cdot\vec{\nabla}\Phi_j + \vec{\nabla}\cdot\phi\xi_j S_j \overline{\overline{\mathrm{K}}}_{kj}\vec{\nabla}x_{kj}\right) + \sum_{k=1}^{n_c}\overline{V}_{tk}\frac{q_k}{V_b}. \tag{6}$$

In this work, an IMPEC-type formulation [34] is used to solve the set of nonlinear equations. In this formulation, the pressure is solved at the new time level using all other variables at the old time level. The new pressure is used to evaluate the mole balance, and then a flash calculation is performed to evaluate the amount and composition of phases at the new time step.

3. NUMERICAL DISCRETIZATION

In order to obtain the approximate equations in EbFVM, each element is divided into sub-control volumes, as shown in Figure 1. Next, the material balance equations and pressure equation (Eq. (1) and (6)) are integrated in time and for each of these sub-control volumes. In this work we consider only the hexahedron element. Figure 1*b* presents a trilinear hexahedron element, sub-control volumes associated with each vertex, and the integration points for each sub-control volume. Integrating each term of Eq. (1), for instance, in space and time for each sub-control volume, and applying the Gauss theorem for the advective and dispersion terms, yields

$$\int_{t,V}\frac{1}{V_b}\frac{\partial N_k}{\partial t}\mathrm{d}t\mathrm{d}V = \int_{t,A}\left(\sum_{j=1}^{n_p} x_{kj}\xi_j\frac{k_{rj}}{\mu_j}\bar{\bar{k}}\cdot\vec{\nabla}\Phi_j + \phi\xi_j S_j\overline{\overline{\mathrm{K}}}_{kj}\cdot\vec{\nabla}x_{kj}\right)\cdot\mathrm{d}\vec{A}\,\mathrm{d}t + \int_{t,V}\frac{q_k}{V_b}\mathrm{d}t\mathrm{d}V, \quad k=1,\ldots,n_c+1. \tag{7}$$

Integrating the first and second terms of Eq. (7), and evaluating the fluid properties through an explicit procedure, the following equations for the above-mentioned terms are obtained:

$$Acc_{m,i} = \frac{Vscv_{m,i}}{V_{b,m}}\left(\left(\frac{N_m}{\Delta t}\right)_i - \left(\frac{N_m}{\Delta t}\right)_i^o\right);\ m=1,N_v;\ i=1,\ldots,n_c+1, \tag{8}$$

$$F_{m,i} = \int_A \sum_{j=1}^{n_p}\left(\lambda_j\xi_j x_{ij}\bar{\bar{k}}\cdot\vec{\nabla}\Phi_j + \phi\xi_j S_j\overline{\overline{K}}_{ij}\cdot\vec{\nabla}x_{ij}\right)\cdot\mathrm{d}\vec{A}$$
$$= \sum_{ip=1}^{3}\left(\sum_{j=1}^{n_p}\xi_j^0 x_{ij}^0\lambda_j^0 k_{nl}\left.\frac{\partial\Phi_j}{\partial x_l}\right|_{ip}A_n + \phi\xi_j^0 S_j^0 K_{ijnl}^0\left.\frac{\partial x_{ij}}{\partial x_l}\right|_{ip}A_n\right);$$
$$m=1,N_v;\ n,l=1,\ldots,3;\ i=1,n_c+1. \tag{9}$$

In the above equations, N_v denotes the number of vertices of each element of the grid and *ip* denotes each integration point located on each of the three surfaces shown in

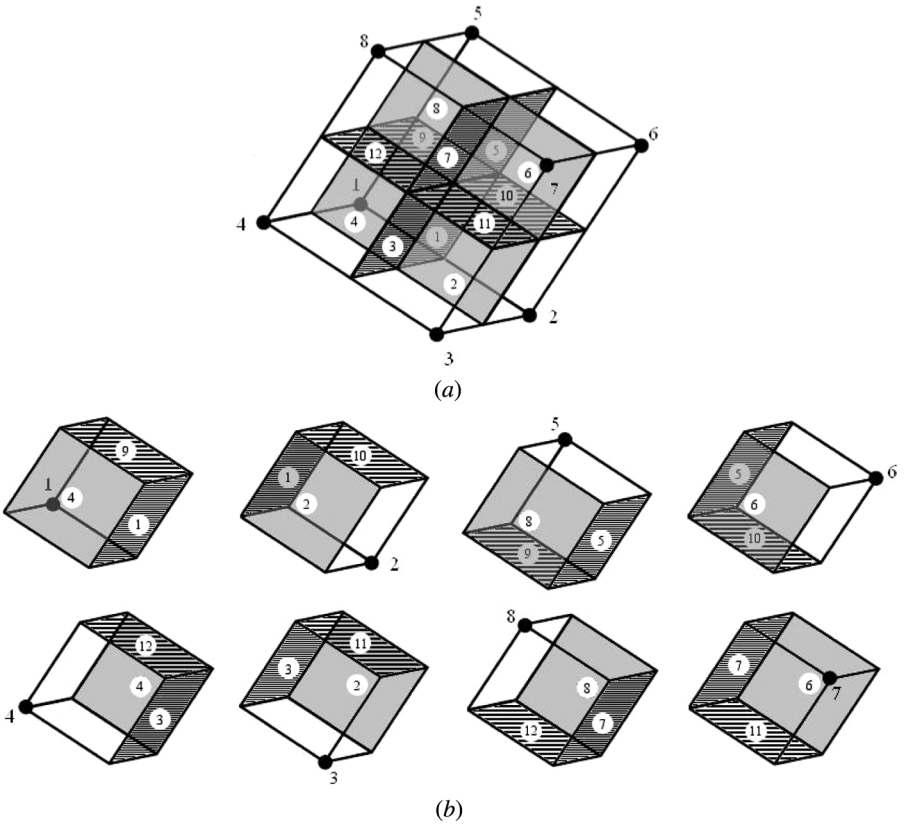

Figure 1. Hexahedron element illustration. (*a*) Whole element; (*b*) all sub-control volumes and their integration points.

Figure 1*b*, for each sub-control volume. A similar procedure is performed for the pressure equation.

Substituting Eqs. (8) and (9) into Eq. (7), the following equation for each element is obtained:

$$Acc_{m,i} + F_{m,i} + q_i = 0; \quad m = 1, \ldots, N_v; \; i = 1, \ldots, n_c + 1. \tag{10}$$

Equation (10) denotes the conservation for each sub-control volume of each element. It is now necessary to assemble the equation of each control volume to obtain the contribution of each sub-control volume that shares the same vertex. This process is similar to assembling of the stiffness global matrix in the finite-element method. Further details of the methodology described above can be found in Marcondes et al. [30].

From Eq. (9), it can be inferred that is necessary to evaluate the fluxes through each integration surface of each sub-control volume and the physical properties ξ_j, x_{ij}, and λ_j. The components of the gradient at each interface are approximated through the shape functions as in Ref [30]; this involves only physical properties evaluated at the vertices of each element. On the other hand, to evaluate the fluxes

of each sub-control volume, it is necessary to extrapolate the physical properties (ξ_j, x_{ij}, and λ_j) from the vertices of the element to each integration surface. In this work, we consider a first-order upwind and a higher-order TVD using two flux-limiter schemes. Instead of evaluating each property separately and then multiplying them, we perform the interpolation for the product of ξ_j, x_{ij}, and λ_j together, as a unique physical property.

The upwind scheme implemented for EbFVM is very similar to the classic upwind scheme used in Cartesian grids. We simply need to find the upwind node for a given interface. Considering for instance the integration point 1 (ip_1), in Figure 1, the product of the physical properties in conjunction with the upwind scheme at ip_1 is given by

$$(x_{ij}\xi_j\,\lambda_j)_{ip1} = \begin{cases} x_{ij,2}\xi_{j,2}\,\lambda_{j,2} & \text{if} \quad \bar{\bar{k}}\cdot\vec{\nabla}\Phi_j\cdot \mathrm{d}\vec{A}|_{ip1} \le 0 \\ x_{ij,1}\xi_{j,1}\,\lambda_{j,1} & \text{if} \quad \bar{\bar{k}}\cdot\vec{\nabla}\Phi_j\cdot \mathrm{d}\vec{A}|_{ip1} > 0, \end{cases} \tag{11}$$

where the normal area considered in Eq. (11) points outward the sub-control volume interface.

For TVD schemes, the flux limiter can be interpreted as a blending key procedure that switches between lower- and higher-order schemes in order to ensure a monotonic solution. For EbFVM, the expression for an arbitrary property is given by Fernandes et al. [26] as

$$\delta_f = \Delta_U + \psi(r_f)\vec{\nabla}\delta_f\cdot\Delta\vec{r}_{Uf}, \tag{12}$$

where the subscript f denotes any integration point where the property needs to be evaluated, $\triangle_U$ is the value of property at the upwind vertex, ψ is the flux-limiter function, $\vec{\nabla}\delta_f$ is the property gradient evaluated at integration point f, $\Delta\vec{r}_{Uf}$ is the distance vector from face f to the upwind vertex, and r_f is the successive slope ratio approximated for EbFVM as

$$r_f = \frac{2\vec{\nabla}\Delta_U\cdot\Delta\vec{r}_{Uf} - \vec{\nabla}\delta_f\cdot\Delta\vec{r}_{Uf}}{\vec{\nabla}\delta_f\cdot\Delta\vec{r}_{Uf}}, \tag{13}$$

where $\vec{\nabla}\Delta_U$ is the property gradient at the upwind vertex.

In our approach, the integration point gradients are evaluated through the shape functions, while the vertex gradients are evaluated using a volumetric mean of the gradients calculated at the vertices of elements that share that vertex, as suggested by Tran et al. [35]. Figure 2 displays all geometric features involved in a 2D calculation; the extension to the 3D grid is straightforward.

Two flux limiters in conjunction with Eq. (12) and (13) are investigated: MINMOD (MM) [36], which is the most diffusive TVD limiter; and Koren's limiter [37], which is a very compressive limiter. The expressions used to evaluate both limiters are given by

$$\text{MINMOD}: \ \psi(r_f) = \max\big(0, \min\big(1, r_f\big)\big), \tag{14}$$

$$\text{Koren}: \ \psi(r_f) = \max\left(0, \min\left(2, 2r_f, \frac{r_f+2}{3}\right)\right). \tag{15}$$

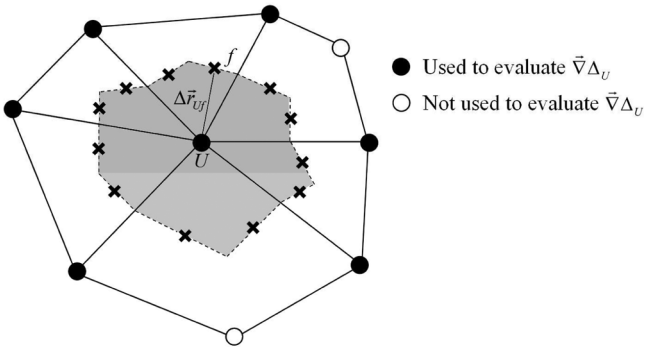

Figure 2. Geometric features of TVD scheme for 2D grid.

Details of other forms of flux limiter, also termed slope limiters, are available in the literature [38, 39].

4. RESULTS

The first case study refers to a 2D tracer injection into a quarter of five-spot configuration. To investigate this case using 3D, a single-element layer grid in the z-direction is used and the gravitational term in the potential of each phase is not considered; therefore, we can perfectly mimic 2D flow using the 3D hexahedron mesh. This is an important case study since we can validate the numerical results with an analytical solution provided by Abbaszadeh-Dehghani and Brigham [40]. In this case the tracer is injected through water to 0.2 pore volume injected (PVI). Subsequently, no tracer is injected but water is continuously injected, at the same volumetric rate, up to 1.6 PVI. The advection and diffusion terms are both considered for this tracer injection problem. The reservoir data are presented in Table 1 and the grid configuration used in this case can be seen in Figure 3; the blue and red arrows denote the injection and production wells, respectively.

The normalized concentration of the tracer produced along time is shown in Figure 4, where the solutions for the upwind, MINMOD, and Koren schemes are compared. As expected, from Figures 4*a* and *b* one may observe that the upwind scheme is less accurate than the other two. Figure 4*c* compares the two TVD schemes, showing that Koren's scheme is superior to MINMOD in terms of numerical accuracy for coarse grids (30×30 and 50×50 elements). However, when the grid is refined the two interpolation functions achieve almost the same tracer concentration profile.

We use the curves shown in Figure 4 to evaluate the L_1-norm error based on time. These errors are shown in Figure 5, where one can see an almost linear trend of the error when the grid is refined. Figure 5 also confirms that both TVD approaches are more accurate than the first-order upwind. It is also verified that for coarse grids the TVD with Koren's flux limiter is more accurate than the TVD with MINMOD. However, when the grid is refined both flux limiters produce the same error; such behavior is verified in Figure 4*c*.

Table 1. Fluid and reservoir data for Case 1

Property	Value
Length, width, thickness	50.292, 50.292, 0.3048 m
Porosity (fraction)	0.2
Water viscosity	2.49×10^{-4} Pa · s
Reservoir pressure	13.79 MPa
Water injection rate	20.39 mol/s
Producer's bottom hole pressure	13.79 MPa
Initial water saturation	1.00
Longitudinal dispersion coefficient	0.2012 m
Transverse dispersion coefficient	0.0201 m
Injected tracer concentration	200 ppm

The second case study is 3D CO_2 flooding into a quarter of five-spot configuration. The reservoir is initially saturated with oil. All reservoir data are presented in Table 2, which also shows the relative permeability parameters of Corey's model [41]. The fluid compositions are shown in Table 3.

Volumetric production rates at surface conditions (289 K and 101.3 kPa) are shown in Figure 6. In this figure, we compare the oil and gas rates using a $20 \times 20 \times 3$ hexahedron element mesh (1,764 volumes) for upwind, MINMOD, and Koren schemes. In order to verify the accuracy of each of these approaches, we also show a refined Cartesian mesh ($60 \times 60 \times 6$—21,600 volumes) solution using the upwind function. Figure 6 shows that the Cartesian grid solution falls between the EbFVM solution with upwind and the TVD solutions. This result suggests that the Cartesian grid solution is somewhat more accurate than the EbFVM upwind solution, which is expected because the Cartesian grid is much finer than that used for EbFVM. However, even when with the element grids being much coarser, the solution for the TVD schemes can be seen as being more accurate than those obtained using the Cartesian grid.

The gas saturation fields for 400 days of production are shown in Figure 7. From this figure, one may observe that Koren's solution is much more compressible than upwind, even for the Cartesian grid. MINMOD is also more compressible than the two upwind solutions obtained with EbFVM and Cartesian grids.

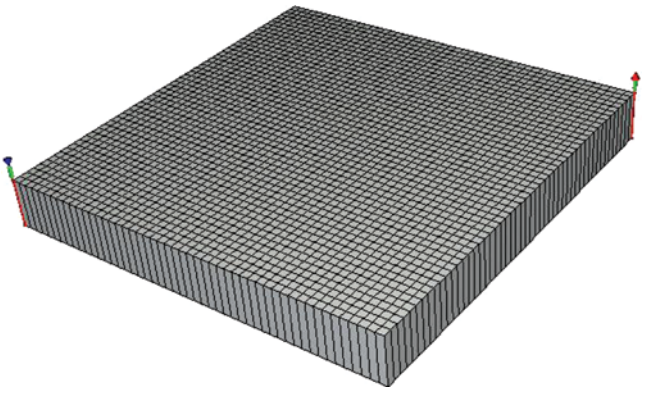

Figure 3. Grid configuration for Case 1—Hexahedron 50×50 elements grid.

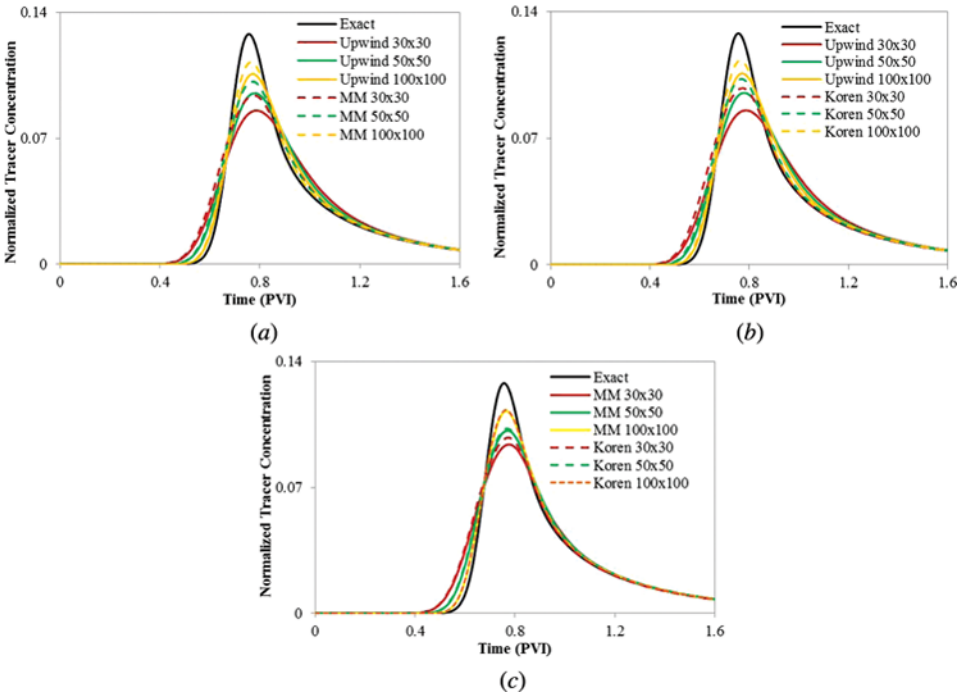

Figure 4. Normalized tracer concentration for Case 1. (*a*) upwind and MINMOD; (*b*) upwind and Koren; and (*c*) MINMOD and Koren.

The third case study is similar to the second, but now an irregularly shaped reservoir is considered. The main purpose of this case is show the functionality of TVD schemes associated with irregular reservoirs. The reservoir in question is shown in Figure 8, where the approximate maximum sizes in each direction are given in feet.

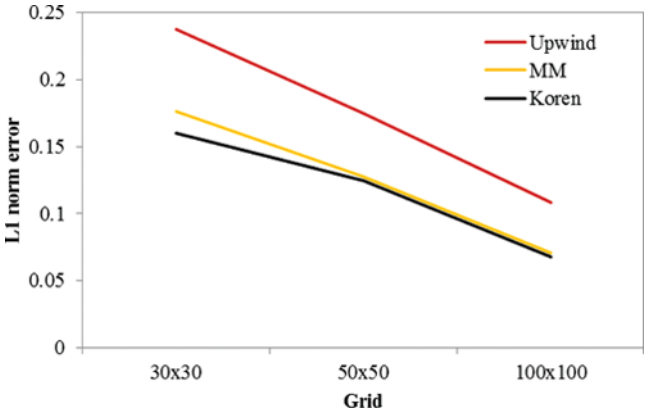

Figure 5. L_1-norm error of normalized tracer concentration produced for Case 1.

Table 2. Reservoir data for Case 2

Property	Value
Length, width, thickness	170.69, 170.69, 3048 m
Porosity (fraction)	0.163
Initial water saturation	0.25
Initial pressure	19.65 MPa
Permeability in *X*-, *Y*-, *Z*-directions	1.974×10^{-13} m^2, 1.974×10^{-13} m^2, 1.974×10^{-14} m^2
Formation temperature	400 K
Gas injection rate	14.16×10^3 m^3/d
Producer's bottom hole pressure	19.65 MPa
Residual saturation (water, oil–water, oil–gas, gas)	0.25, 0.2, 0.2, 0.05
Relative permeability end points (water, oil, gas)	1.0, 0.7, 0.3
Relative permeability exponents (water, oil–water, oil–gas, gas)	1.5, 2.5, 2.5, 2.5

Table 3. Fluid composition data for Case 2

Component	Initial reservoir composition	Injection fluid composition
CO_2	0.0077	0.96
C_1	0.2025	0.01
$C_{2\text{-}3}$	0.1180	0.01
$C_{4\text{-}6}$	0.1484	0.01
$C_{7\text{-}14}$	0.2863	0.01
$C_{15\text{-}24}$	0.1490	—
C_{25+}	0.0881	—

Oil and gas production rates at standard surface conditions are shown in Figure 9. From Figure 9*a*, it will be seen that the oil rate for the finer grid using upwind increases, as it does for the TVD functions investigated. Although this change in oil rate is not large, Figure 9*b* shows wider changes for gas rate. From Figure 9*b*, one can clearly see that the gas production rate for the finer grid using upwind approaches that of the TVD solutions. As expected, these results show that the TVD scheme implemented in this work is more accurate than the upwind scheme, even for irregular grids.

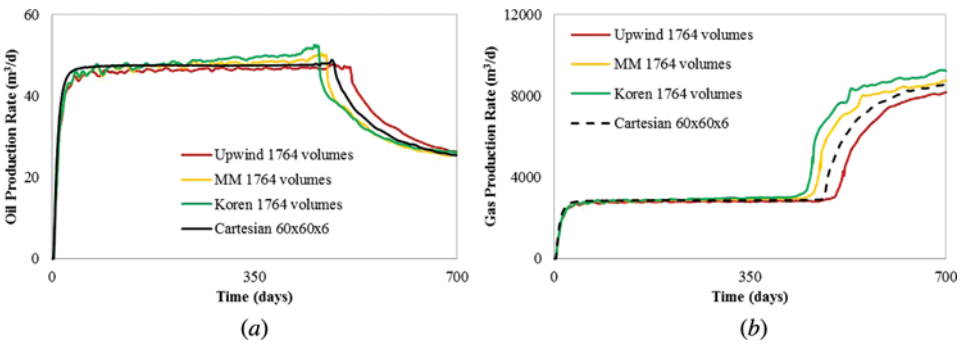

Figure 6. Volumetric production rates at surface condition for Case 2. (*a*) Oil; and (*b*) gas.

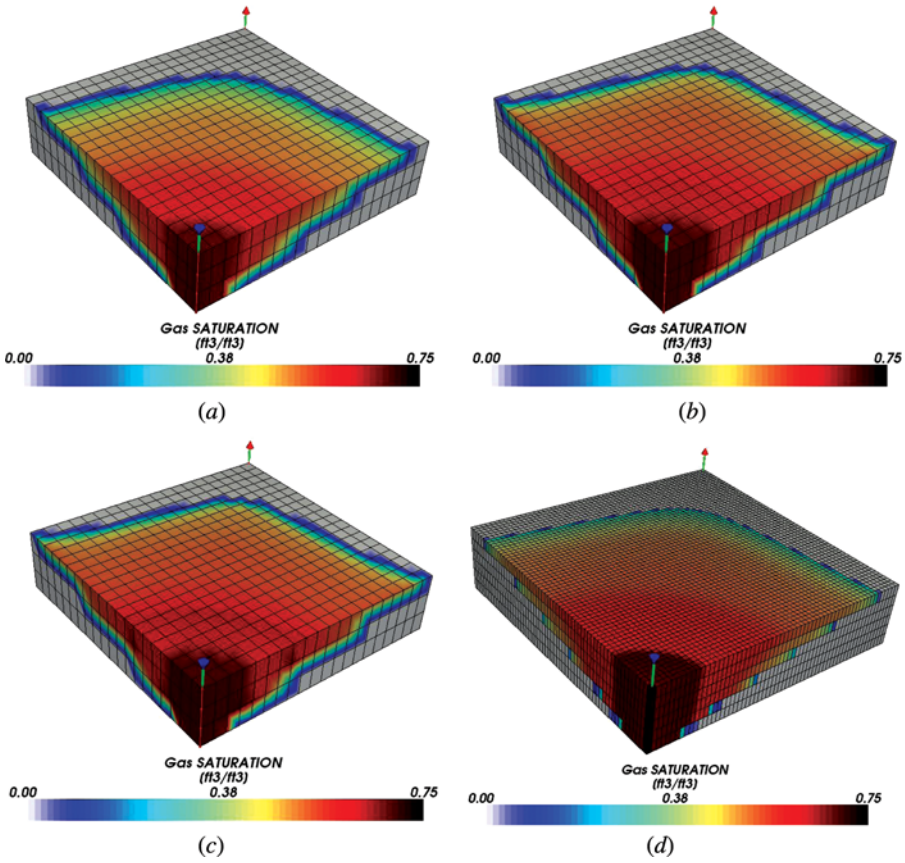

Figure 7. Gas saturation field at 400 days for Case 2. (*a*) Upwind 1,764 vertices; (*b*) MINMOD 1,764 vertices; (*c*) Koren 1,764 vertices; and (*d*) Cartesian $60 \times 60 \times 6$.

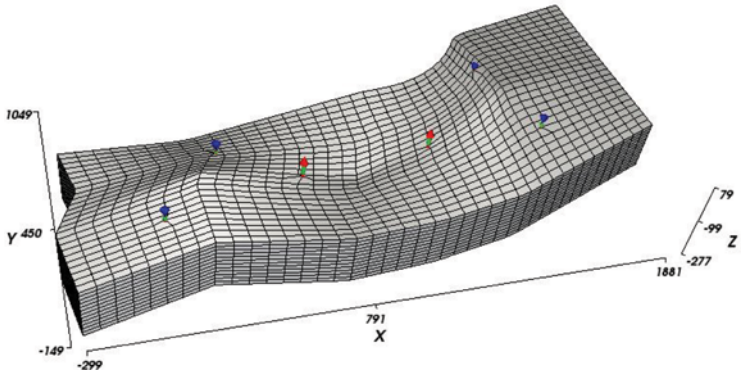

Figure 8. Grid configuration used for Case 3—hexahedron grid (13,858 vertices; 12,000 elements).

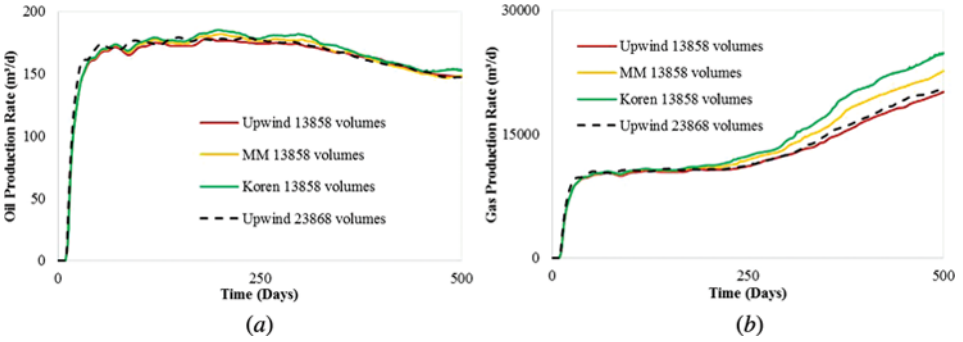

Figure 9. Volumetric production rates at surface condition for Case 3. (*a*) Oil; and (*b*) gas.

The gas saturation fields at 500 days of production are shown in Figure 10. From this figure, no major differences are noted in the gas front for all grids and interpolation functions investigated.

In order to better observe the effect of interpolation functions, we show the gas saturation field again at 500 days for a plane-cut that passes through two of the injection wells. One may observe that the TVD associated with the Koren flux limiter is the most compressible, followed by TVD with MINMOD (Figure 11).

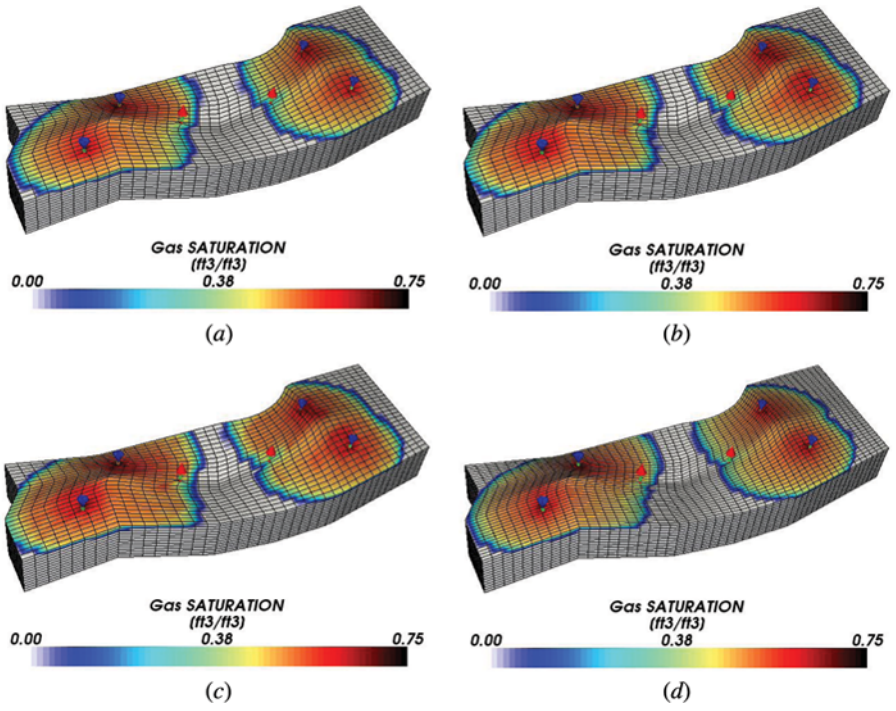

Figure 10. Gas saturation field at 500 days for Case 3. (*a*) Upwind 13,858 vertices; (*b*) MINMOD 13,858 vertices; (*c*) Koren 13,858 vertices; and (*d*) upwind 23,868 vertices.

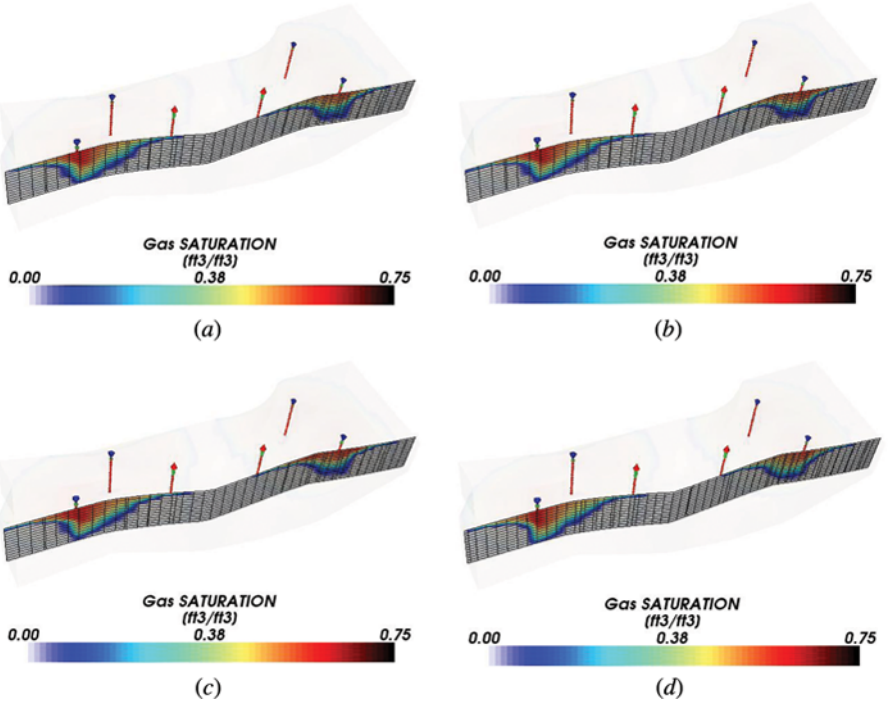

Figure 11. Gas saturation field at 500 days for Case 3. (*a*) Upwind 13,858 vertices; (*b*) MINMOD 13,858 vertices; (*c*) Koren 13,858 vertices; and (*d*) upwind 23,868 vertices.

The final case study investigated consists of a gas flooding into an irregularly shaped reservoir which contains a section with negligible absolute permeability (considered as dead grid blocks). The reservoir fluid is characterized by six hydrocarbon

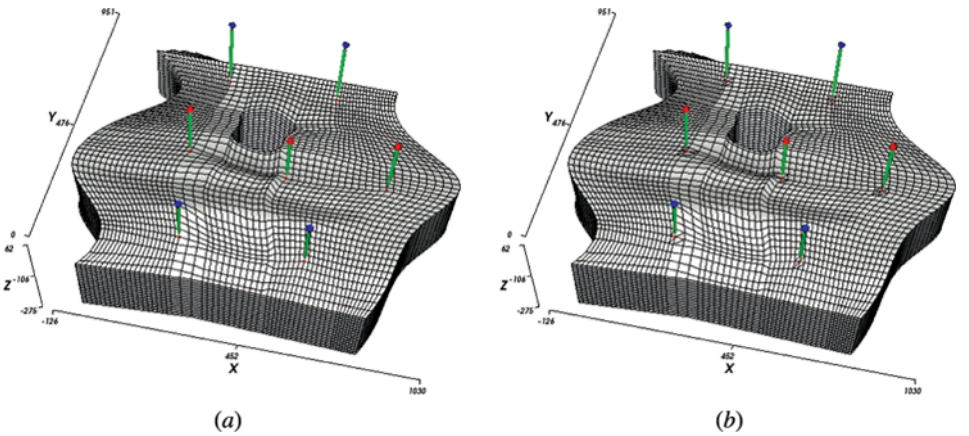

Figure 12. Grid configurations used for Case 4. (*a*) Hexahedron grid (41,392 vertices; 36,975 elements); and (*b*) hybrid grid (42,232 vertices; 4,200 tetrahedrons; 35,715 hexahedrons; 4,200 pyramids).

Table 4. Reservoir data for Case 4

Property	Value
Porosity (fraction)	0.35
Initial water saturation	0.17
Initial pressure	10.34 MPa
Permeability in all directions	9.869×10^{-15} m^2
Formation temperature	344.26 K
Gas injection rate	28.32×10^3 m^3/d
Producer's bottom hole pressure	8.96 MPa
Residual saturations (water, oil–water, oil–gas, gas)	0.3, 0.1, 0.1, 0
Relative permeability end points (water, oil, gas)	0.4, 0.9, 0.9
Relative permeability exponents (water, oil–water, oil–gas, gas)	3.0, 2.0, 2.0, 2.0

Table 5. Fluid composition data for Case 4

Component	Initial reservoir composition	Injection fluid composition
C_1	0.5000	0.7700
C_3	0.0300	0.2000
C_6	0.0700	0.0100
C_{10}	0.2000	0.0100
C_{15}	0.1500	0.0050
C_{20}	0.0500	0.0050

components and the reservoir initially contains only oil. The reservoir shape and grids are shown in Figure 12.

The reservoir data are shown in Table 4 and the fluid composition in Table 5. The relative permeability parameters for Corey's model [41] are also given in Table 4.

Figure 13 shows the oil and gas production rates at surface conditions for case 4. Although the differences in curves for oil rates are negligible, one may observe major differences in gas rates (Figure 13*b*). From Figure 13*b*, one can clearly see that the finer grid using upwind approaches the TVD solutions, suggesting that the TVD approaches yield more accurate results than upwind.

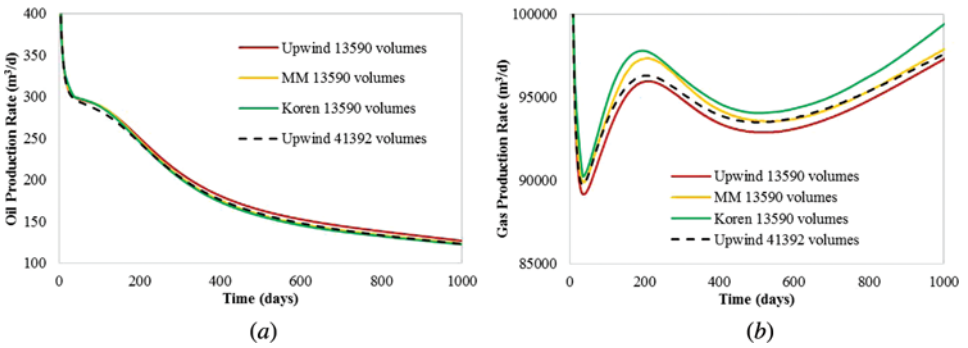

Figure 13. Volumetric production rates at surface condition for Case 4. (*a*) Oil; and (*b*) gas.

5. CONCLUSIONS

In this work, a TVD scheme using two flux limiters and an upwind scheme were implemented in conjunction with a cell–vertex approach for compositional reservoir simulation. The schemes were tested for several case studies and were validated through the use of both analytical and available numerical solutions using Cartesian grids under the upwind scheme. The obtained results for the TVD scheme using both flux limiters demonstrated that the tested and implemented scheme can accurately overcome numerical dispersion, and that it is a good option for use in conjunction with irregular grids.

FUNDING

The authors would like to acknowledge the PETROBRAS S/A Company for their financial support of this work. Also, the authors would like to thank the ESSS Company for providing Kraken® to pre- and post-process the results. Finally, Francisco Marcondes would like to acknowledge CNPq (The National Council for Scientific and Technological Development of Brazil) for its financial support through grant no. 305415/2012-3.

REFERENCES

1. B. R. Baliga and S. V. Patankar, A New Finite-Element Formulation for Convection-Diffusion Problems, *Numer. Heat Transfer*, vol. 3, no. 4, pp. 393–409, 1980.
2. C. R. Maliska, *Computational Heat Transfer and Fluid Mechanics*, 2nd ed., pp. 322–323, LTC, Rio de Janeiro, 2004 (in Portuguese).
3. C. Prakash, An Improved Control Volume Finite-Element Method for Heat and Mass Transfer, and for Fluid Flow Using Equal-Order Velocity-Pressure Interpolation, *Numer. Heat Transfer*, vol. 9, no. 3, pp. 253–276, 1986.
4. G. D. Raithby, A Critical Evaluation of Upstream Differencing Applied to Problems Involving Fluid Flow, *Comput. Methods Appl. Mech. Eng.*, vol. 9, no. 1, pp. 75–103, 1976.
5. G. D. Raithby, Skew Upstream Differencing Schemes for Problems Involving Fluid Flow, *Comput. Methods Appl. Mech. Eng.*, vol. 9, 2, pp. 153–164, 1976.
6. Y. A. Hassan, J. G. Rice, and J. H. Kim, A Stable Mass-Flow-Weighted Two-Dimensional Skew Upwind, *Numer. Heat Transfer*, vol. 6, no. 4, pp. 395–408, 1983.
7. G. E. Schneider, M. J. Raw, and A Skewed, Positive Influence Coefficient Upwinding Procedure for Control-Volume-Based Finite-Element Convection-Diffusion Computation, *Numer. Heat Transfer*, vol. 9, no. 1, pp. 1–26, 1986.
8. C. R. Swaminathan and V. R. Voller, Streamline Upwind Scheme for Control-Volume Finite Elements, Part I: Formulations, *Numer. Heat Transfer, Part B*, vol. 22, no. 1, pp. 95–107, 1992.
9. C. R. Swaminathan and V. R. Voller, Streamline Upwind Scheme for Control-Volume Finite Elements, Part II: Implementation and Comparison with the SUPG Finite-Element Scheme, *Numer. Heat Transfer, Part B*, vol. 22, no. 1, pp. 109–124, 1992.
10. A. N. Brooks and T. J. R. Hughes, Streamline Upwind/Petrov–Galerkin Formulations for Convection Dominated Flows with Particular Emphasis on the Incompressible Navier–Stokes Equations, *Comput. Methods Appl. Mech. Eng.*, vol. 32, no. 1–3, pp. 199–259, 1982.

11. B. van Leer, Towards the Ultimate Conservative Difference Scheme. V - A Second-Order Sequel to Godunov's Method, *J. Comput. Phys.*, vol. 32, no. 1, pp. 101–136, 1979.
12. A. Harten, High Resolution Schemes for Hyperbolic Conservation Laws, *J. Comput. Phys.*, vol. 49, no. 3, pp. 357–393, 1983.
13. P. K. Sweby, High Resolution Schemes Using Flux Limiters for Hyperbolic Conservation Laws, *SIAM J. Numer. Anal.*, vol. 21, no. 5, pp. 995–1011, 1984.
14. P. L. Roe, Some Contributions to the Modelling of Discontinuous Flows, Summer Seminar on Applied Mathematics, *Proceedings of the 15th Summer Seminar on Applied Mathematics*, La Jolla, USA, 1983.
15. S. R. Chakravarthy and S. Osher, High Resolution Applications of the Osher Upwind Scheme for the Euler Equations, Computational Fluid Dynamics, *Proceedings of the 6th Computational Fluid Dynamics Conference*, Danvers, MA, pp. 363–372, 1983.
16. P. Lax and B. Wendroff, Systems of Conservation Laws, *Commun. Pure Appl. Math.*, vol. 13, no. 2, pp. 217–237, 1960.
17. R. F. Warming and R. M. Beam, Upwind Second Order Difference Schemes and Applications in Aerodynamics, *AIAA J.*, vol. 14, no. 9, 1976.
18. C. W. S. Bruner and R. W. Walters, Parallelization of the Euler Equations on Unstructured Grids, AIAA paper 97–1894, 1995.
19. C. W. S. Bruner, Parallelization of the Euler Equations on Unstructured Grids, Ph.D. dissertation, Department of Aerospace Engineering, Virginia Polytechnic Institute and State University, Blacksburg, VA, 1996.
20. M. S. Darwish and F. Moukalled, TVD Schemes for Unstructured Grids, *Int. J. Heat Mass Transfer*, vol. 46, no. 4, pp. 599–611, 2003.
21. C. M. Rhie and W. L. Chow, Numerical Study of the Turbulent Flow Past and Airfoil with Trailing Edge Separation, *AIAA J.*, vol. 21, no. 11, pp. 1525–1532, 1983.
22. C. O. E. Burg, High-Order Variable Extrapolation for Unstructured Finite Volume RANS Solvers, AIAA Paper 2005–4999, *AIAA Computational Fluid Dynamics 2005, 17th AIAA Computational Fluid Dynamics Conference*, Toronto, Canada, 2005.
23. L. Li, H. Liao, and L. Qi, An Improved r-Factor Algorithm for TVD Schemes, *Int. J. Heat Mass Transfer*, vol. 51, no. 3–4, pp. 610–617, 2008.
24. J. Hou, F. Simons, and R. Hinkelmann, Improved Total Variation Diminishing Schemes for Advection Simulation on Arbitrary Grids, *Int. J. Numer. Methods Fluids*, vol. 70, no. 3, pp. 359–382, 2011.
25. J. Hou, F. Simons, and R. Hinkelmann, A New TVD Method for Advection Simulation on 2D Unstructured Grids, to be published on *Int. J. Numer. Methods Fluids*, vol. 71, no. 10, pp. 1260–1281, 2013.
26. B. R. B. Fernandes, F. Marcondes, and K. Sepehrnoori, Investigation of Several Interpolation Functions for Unstructured Meshes in Conjunction with Compositional Reservoir Simulation, *Numer. Heat Transfer, Part A*, vol. 64, no. 12, pp. 974–993, 2013.
27. Y.-B. Chang, Development and Application of an Equation of State Compositional Simulator, Ph.D. thesis, Department of Petroleum and Geosystems Engineering, The University of Texas at Austin, Austin, TX, 1990.
28. Y.-B. Chang, G. A. Pope, and K. Sepehrnoori, A Higher Order Finite-Difference Compositional Simulator, *J. Pet. Sci. Eng.*, vol. 5, no. 1, pp. 35–50, 1990.
29. F. Marcondes and K. Sepehrnoori, An Element-Based Finite Volume-Method Approach for Heterogeneous and Anisotropic Compositional Reservoir Simulation, *J. Pet. Sci. Eng.*, vol. 73, no. 1–2, pp. 99–106, 2010.
30. F. Marcondes, L. O. S. Santos, A. Varavei, and K. Sepehrnoori, A 3D Hybrid Element-based Finite-Volume Method for Heterogeneous and Anisotropic Compositional Reservoir Simulation, *J. Pet. Sci. Eng.*, vol. 108, pp. 342–351, 2013.

31. L. O. S. Santos, F. Marcondes, and K. Sepehrnoori, A 3D Compositional Miscible Gas Flooding Simulator with Dispersion Using Element-Based Finite-Volume Method, *J. Pet. Sci. Eng.*, vol. 112, pp. 61–68, 2013.
32. D. Y. Peng and D. B. Robinson, *The Characterization of the Heptanes and Heavier Fractions for the GPA Peng–Robinson Programs*, Gas Processors Association, Tulsa, OK, 1978.
33. D. R. Perschke, Equation of State Phase Behavior Modelling for Compositional Simulator, Ph.D. thesis, Department of Petroleum and Geosystems Engineering, The University of Texas at Austin, Austin, TX, 1988.
34. G. Àcs, S. Doleschall, and E. Farkas, General Purpose Compositional Model, *SPE J.*, vol. 25, pp. 543–553, 1985.
35. L. D. Tran, C. Masson, and A. Smaïli, A Stable Second-Order Mass-Weighted Upwind Scheme for Unstructured Meshes, *Int. J. Numer. Methods Fluids*, vol. 51, no. 7, pp. 749–771, 2006.
36. P. L. Roe, Some Characteristic-Based Schemes for the Euler Equations, *Ann. Rev. Fluid Mech.*, vol. 18, pp. 337–365, 1986.
37. B. Koren, A Robust Upwind Discretization Method for Advection, Diffusion and Source Terms, in C. B. Vreugdenhil and B. Koren (eds.), *Numerical Methods for Advection-Diffusion Problems, Notes on Numerical Fluid Mechanics*, vol. 45, pp. 117–138, Vieweg, Braunschweig, 1993.
38. M. Berger, M. J. Aftomis, and S. M. Murman, Analysis of Slope Limiters on Irregular Grids, *AIAA Aerospace 2005, 43rd AIAA Aerospace Meeting*, Reno, NV, 2005.
39. B. F. Sanders and S. F. Bradford, Impact of Limiters on Accuracy of High-Resolution Flow and Transport Models, *J. Eng. Mech.*, vol. 132, no. 1, pp. 87–98, 2006.
40. M. Abbaszadeh-Dehghani and W. E. Brigham, Analysis of Well-to-Well Tracer Flow to Determine Reservoir Layering, *J. Pet. Technol.*, vol. 36, pp. 1753–1762, 1984.
41. A. T. Corey, *Mathematics of Immiscible Fluids in Porous Media*, Water Resources Publication, Littleton, CO, USA, 1986.